LUND UNIVERSITY
Faculty of Science

Characterization of biomass pyrolysis and gasification using Raman Spectroscopy

Henrik Johansson

Thesis submitted for the degree of Master of Science
Project duration: 4 months

Supervised by Christian Brackmann

Department of Physics
Division of Combustion Physics
May 2018

Abstract

This thesis examines the emissions formed during pyrolysis and gasification of lignocellulosic biomass in pellet form, using vibrational Raman spectroscopy. Seven different samples are studied during the pyrolysis process and six of these are also studied during gasification. For pyrolysis, the sample is placed into the center of a cruciform aluminum pipe, flushed with Ar, at room temperature. The Raman signal is then recorded as the pipe is heated up to ∼770 K, at a rate of ∼38 K/min. The gasification measurements are performed in a similar manner, with the addition of O_2, to a concentration of ∼4%, into the pipe. During pyrolysis, the samples were shown to emit traces of some species containing an -NH_2 group at temperatures below 450 K, various hydrocarbons at temperatures above this, and H_2O was emitted during the entire process. Data for the gasification process showed strong emissions from several >C=O groups between temperatures 450 K and 550 K, CO_2 and several hydrocarbons from temperatures of 450 K and above, and CO above temperatures of 500 K.

Acronyms and abbreviations

LIF	Laser-induced fluorescence
RISE	Research Institute of Sweden
RS	Raman Spectroscopy
SNR	Signal-to-noise ratio

Contents

Chapter 1

Introduction

In the modern energy supply sector, the most common way to extract energy is through combustion processes of various materials. These materials may be coal, oil, wood, municipal waste or natural gas [1]. Due to their big impact on global warming, fossil fuels - such as coal and oil - are continuously being replaced by renewable energy sources, such as biomass, which is considered CO_2 neutral.

As of 2015, biomass constituted 9.7% of the worlds total primary energy supply and 24.5% of the total energy supply in Sweden, as shown in the two diagrams in Fig. 1.1 [1, 2]. Most of this biomass - in Sweden and worldwide - consists of wood and residues from the wood, pulp and paper industries. While much of it is burned as is, a lot can be won by using different treatment processes to increase the energy density of the fuel. Examples of these kind of treatment processes are the two thermal processes pyrolysis and gasification, by which a large part of the solid fuel is converted into gaseous form.

This project looks at the gas mixture resulting from the two processes mentioned above. The aim is to characterize the resulting gas mixtures using Raman Spectroscopy (RS) and thereby learn how the ratio between the different constituent gases and contaminants varies between the two processes. Hopefully, in the future, this will lead to a wider use of biofuels that have higher energy density and emit less harmful substances into the environment.

1.1 Biomass

Biomass is a collective name for a range of organic matter used as fuel to supply energy. The term comprises materials such as wood, residues from wood, pulp and paper industries, energy crops, agricultural residues and municipal waste [2, 3]. These materials can either be directly combusted in a steam boiler for heat or converted into other forms, mainly via three different types of processes; biochemical, chemical and thermal.

Biochemical processes utilize microorganisms to break down the biomass into fuels such as biogas and bioethanol. Chemical conversion processes involve gasification, where

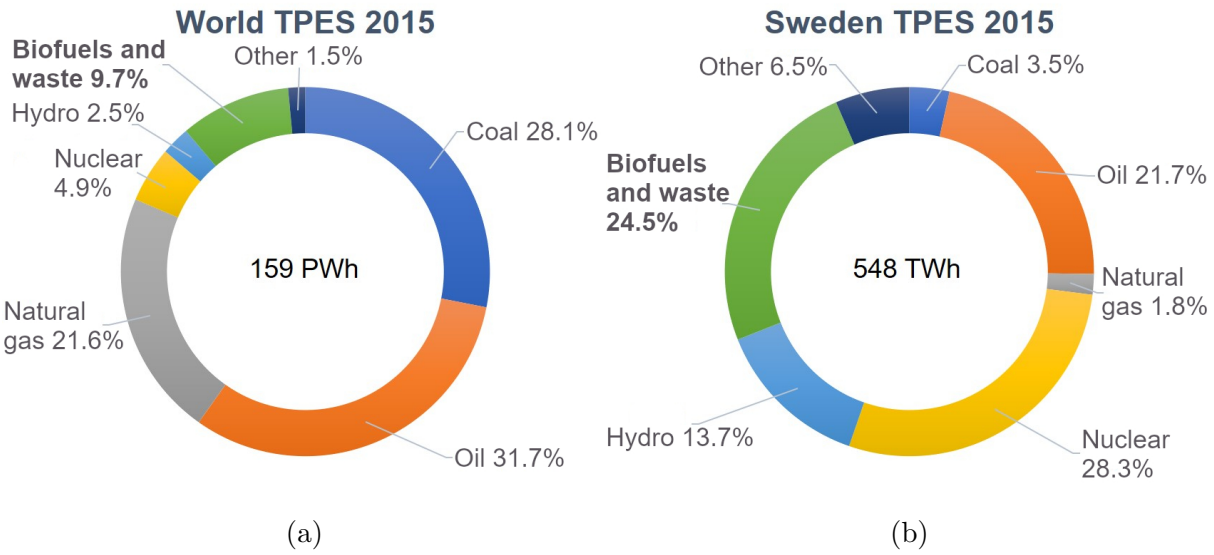

(a) (b)

Figure 1.1: *Diagrams showing the Total Primary Energy Supply (TPES) 2015 (a) worldwide and (b) in Sweden.*

the resulting gas mixture is then further processed via methods such as Fischer-Tropsch synthesis, turning it into liquid hydrocarbons [4]. Thermal conversion processes include three main methods called pyrolysis, gasification and liquefaction, in which solid biomass is converted into gaseous or liquid fuel. Only the two thermal processes resulting in gaseous fuel, pyrolysis and gasification, will be treated here.

Before undergoing thermal conversion, the biomass is usually dried, decreasing the moisture content from ∼50% to ∼12%, thus increasing the heating value of the biomass. The biomass can then be compressed into pellets or briquettes, to make it more manageable.

1.1.1 Pyrolysis

Pyrolysis of biomass is performed by heating up the chosen material to a temperature within a range of 470-770 K in an inert environment, e.g., N_2 or Ar. An example of a pyrolysis gasifier can be seen in the schematic drawing displayed in Fig. 1.2a, showing Ar being injected from the sides and fuel supplied from the top. Before being subject to the pyrolysis process itself, the fuel first goes through a drying process, and the resulting pyrolysis gas is then extracted from the side close to the bottom. The resulting gas mixture consisting mainly of CH_4, C_2-hydrocarbons, and larger hydrocarbons - referred to as volatiles and tar. Besides the gas mixture, the pyrolysis end product also consists of a fluid known as bio-oil - consisting mostly of tar and water - and a solid char, consisting of carbon and ash. The concentration of each of these products depends on several factors: feedstock, temperature, pressure, residence time in the reaction zone, and heating rate [5, 6].

The goal of biomass pyrolysis is usually to maximize the yield of either the bio-oil - using fast or flash pyrolysis - or the char - using slow pyrolysis, while maximization of the gas yield is less common [7]. Maximization of the gas yield is usually achieved in the higher end of the pyrolysis temperature range with the aid of catalysts, such as K_2CO_3, CaO, and Cr_2O_3. Except for hydrocarbons, the gas is also likely to contain other contaminants, such as alkali metals (K and Na) - which cause erosion - Cl in the form of HCl and S in the form of H_2S, both of which will cause corrosion to the pyrolysis equipment unless treated [8].

1.1.2 Gasification

Biomass gasification takes place at higher temperatures than pyrolysis, usually in the range of 1070-1220 K, in an environment where oxygen is available, but the concentration is heavily suppressed (20-30% of what is needed for complete combustion). This means that the material will undergo both pyrolysis - when the temperature lies in the range 470-770 K - and partial oxidation, due to the availability of oxygen [5, 9]. A schematic drawing of a gasifier can be seen in Fig. 1.2b, showing air being injected from the bottom of the gasifier and fuel from the top. As can be seen, in this example, the fuel first goes through a drying process, then pyrolysis reduction, before the partial oxidation process. The resulting gas is then extracted from the side of the gasifier, close to the top.

Regarding the resulting products, these are virtually the same as for the pyrolysis process, although the yield distribution differs. In particular, the gas mixture yield is significantly higher - hence the name of the process - and, presumably, has a different distribution of the gas constituents, with larger amounts of smaller hydrocarbons, due to the partial oxidation process. Similar to pyrolysis, the gas mixture will also, most likely, contain non-ignorable amounts of tar, as well as other contaminants, in the form of alkali metals, Cl, S, as well as NH_3 and HCN (both of which form harmful NO_X during combustion) [8, 10]. Therefore, the gas will normally be required to undergo a cleaning process (e.g. condensation) before utilization as fuel, as to avoid erosion, corrosion and the formation of environmentally hazardous compounds.

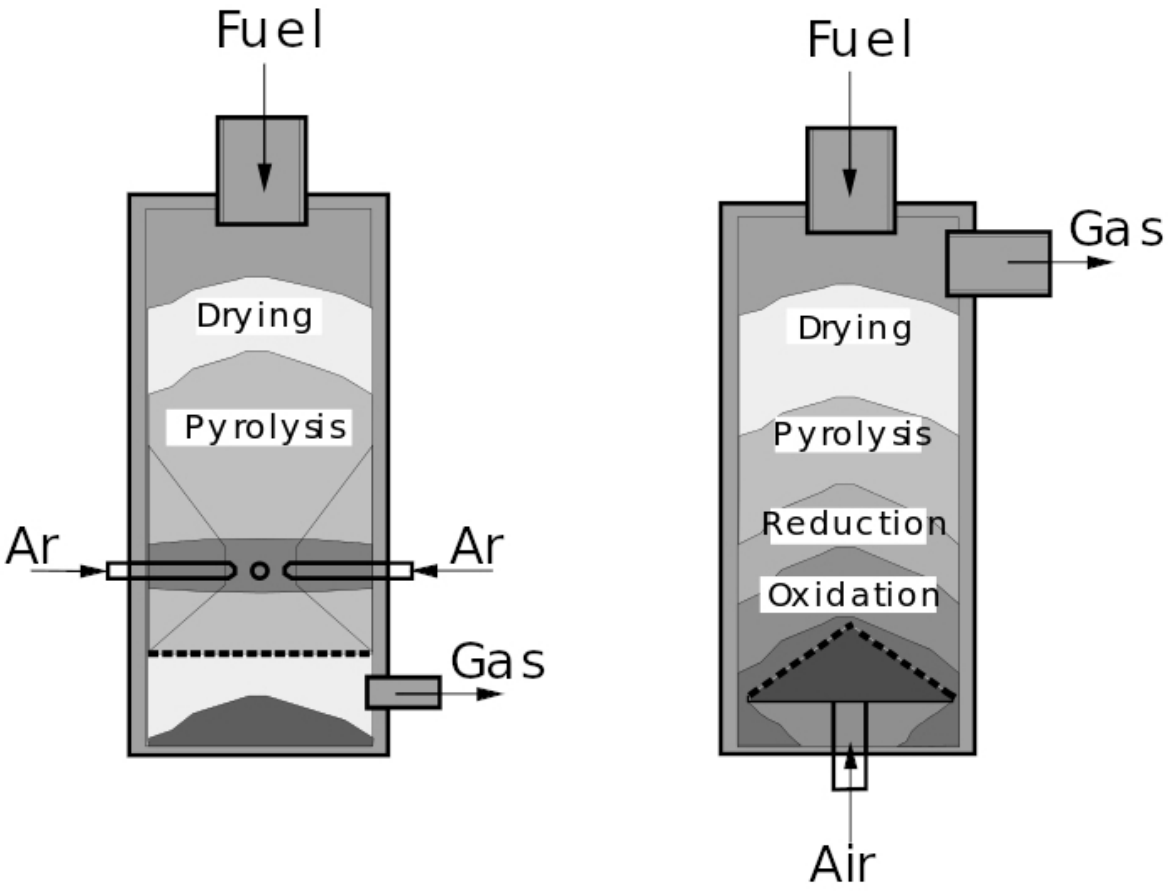

(a) (b)

Figure 1.2: *Two examples of setups used for thermal conversion of biomass, one for (a) pyrolysis and one for (b) gasification. In (a), Ar is injected from the sides while the fuel is supplied from the top. During the process, the fuel is first dried before being subjected to pyrolysis. The resulting gas mixture is then extracted from the side, close to the bottom. In (b), air is injected from the bottom and the fuel is supplied from the top. Here, the fuel is first dried, then goes through pyrolysis and reduction before the oxidation process, and the resulting gas mixture is extracted from the side, close to the top [11].*

Chapter 2

Theory of Raman spectroscopy

The principle of RS builds on the phenomenon of Raman scattering, which is an inelastic scattering process between light and molecules. When a photon interacts with a molecule in an inelastic scattering process, energy is transferred. This is described theoretically by the molecule being excited into a virtual state. The excitation can be exclusively vibrational, exclusively rotational, or a combination of the two, vibrational-rotational. To deexcite, the molecule will then emit a photon with either lower or higher energy than the incoming photon, depending on whether the molecule was in its ground state or already in an excited state before the process started. This photon is known as a Stokes photon or an anti-Stokes photon, respectively, and its frequency serves as a unique fingerprint for every molecular bond [12, 13]. A representation of the vibrational Raman scattering process can be seen in Fig. 2.1, displaying the difference between the scattering of the Stokes and the anti-Stokes photon.

In a classical sense, when the molecule experiences the electric field from the incoming, polarized laser light, it will start to vibrate or rotate, depending on the frequency of the field. However, not all molecules are Raman active. In order to be so, the molecule needs to be able to be polarized by the vibration or rotation caused by the incoming electric field. Also, molecules that are vibrational Raman active are not necessarily rotational Raman active; e.g., CH_4 - a so called spherical top molecule - is not rotational Raman active, since its polarizability surface is spherical, i.e., polarized in the radial direction. It is, however, vibrational Raman active. A simple drawing, illustrating such a spherical top molecule is displayed in Fig. 2.2. Quantum mechanical selection rules also apply, where the rotational transitions must obey $\Delta J = \pm 2$, and the vibrational transitions must obey $\Delta v = 0, \pm 1, \pm 2, ...$. The form of RS presented here (i.e. vibrational) concerns only the $\Delta v = \pm 1$, $\Delta J = 0$ transitions.

After deexcitation, photons are emitted from the molecules in a toroid pattern - in all directions except for the one along the polarization axis of the incoming photon, as illustrated in Fig. 2.3 - and, often, the Raman signal is collected at an angle perpendicular to that of the incoming photon. This signal can then be focused onto the entrance slit

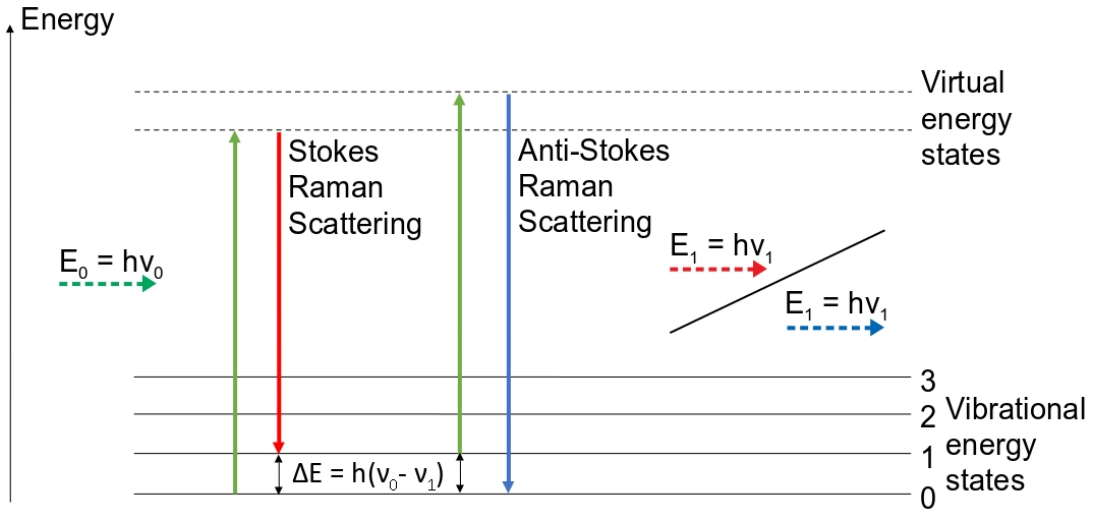

Figure 2.1: *Schematic representation of the vibrational Raman scattering process. An incoming photon interacts with a molecule, exciting it into a virtual energy state. Depending on if the molecule was in its ground state or an excited vibrational state before the process started, it will then emit either a Stokes signal or an anti-Stokes signal when deexciting into another state than the original one.*

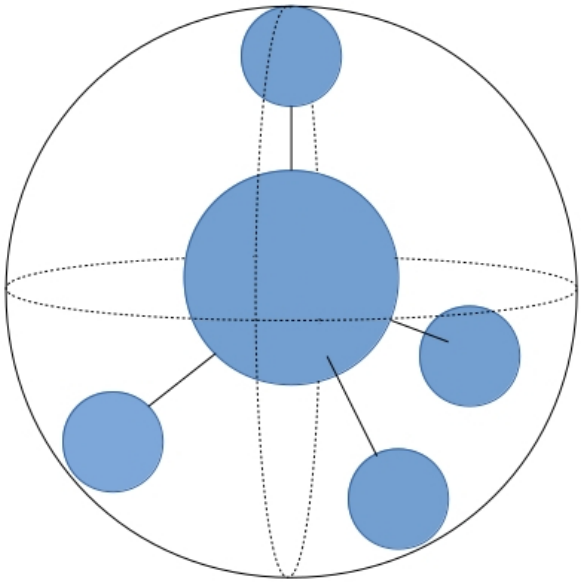

Figure 2.2: *Schematic drawing showing an example of a spherical top molecule, such as CH_4. The encapsulating sphere represents the polarizability surface.*

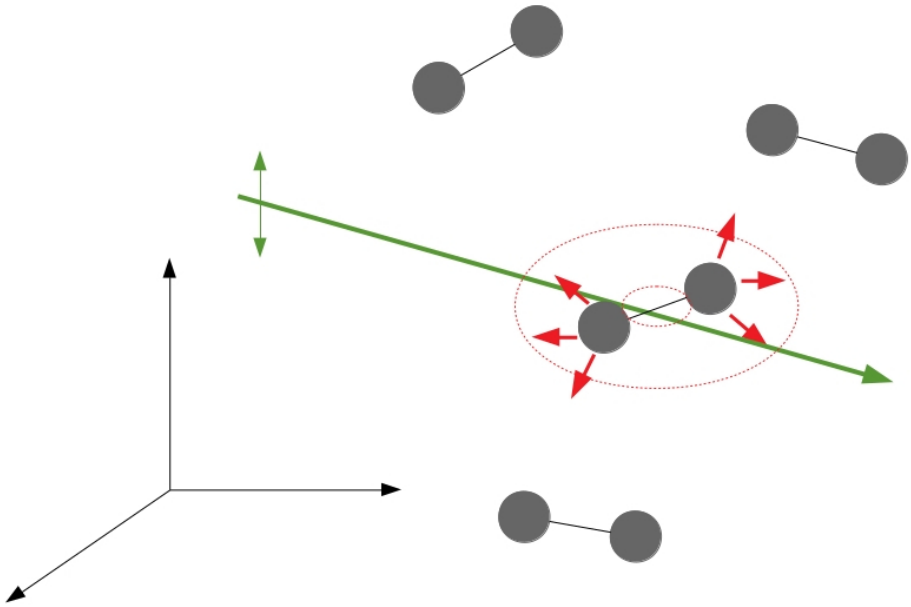

Figure 2.3: *Schematic drawing of the Raman signal emission. Photons of the vertically polarized laser beam interact with a diatomic molecule, which subsequently emits photons of reduced energy in a toroid pattern.*

of a grating spectrometer and directed to a CCD camera so that a spectrum can be recorded. The recorded signal strength, proportional to the scattered Raman power, P_r, is determined by

$$P_r = P_i n \left(\frac{\partial \sigma}{\partial \Omega} \right) \Omega \ell \epsilon, \tag{2.1}$$

where P_i is the incident laser power, n is the number density of scattering species, $\left(\frac{\partial \sigma}{\partial \Omega}\right)$ is the differential Raman cross section, which depends on the polarization, therefore, also the signal is polarization dependent. The signal is also determined by Ω, which is the solid detection angle, ℓ, which is the sampling volume extent, and ϵ, which is the collection efficiency of the detection apparatus.

RS is often employed as an *in situ*, non-intrusive, diagnostic tool in combustion processes and gases [10, 12, 14]. The advantage of using RS over other methods is that it offers non-intrusive, instant, multi-species detection, while simultaneously providing information about the concentrations of the different species (cf. Eq. 2.1), since the Raman signal strength is directly proportional to the number of scattering species. Compared to other scattering processes, such as Rayleigh scattering, or Laser-Induced Fluorescence (LIF), the Raman scattering is much weaker, having a cross section that is up to 10^4 times lower than the cross section of Rayleigh scattering and up to 10^{10} times weaker than the

cross section of LIF. However, if the setup allows, the Raman signal strength can easily be amplified by letting the laser beam pass multiple times through the probe volume [15].

Chapter 3

Experimental

For Raman spectroscopy measurements during pyrolysis, the sample needs to be heated up in an inert environment, through which a laser beam is able to propagate. At the same time, the emitted, non-collimated Raman signal would have to be easily collected and recorded. For gasification, the conditions need to be similar to the ones mentioned above, and, in addition, the concentration of O_2 in the environment needs to be easily controlled.

3.1 Laser setup & signal detection

The measurements presented in this thesis were performed using a pulsed Edgewave HD40I-OE Nd:YAG laser, frequency-doubled from 1064 nm to 532 nm to reduce fluorescence, with a maximum output power of 100 W, a pulse energy of 10 mJ and a pulse duration of 12 ns. During measurements, the laser was controlled by a BNC Model 575 external pulse generator, operating at a frequency of 1 kHz, giving an output power of 10 W. The benefit of using a pulsed laser beam is that it, in combination with external ICCD intensifier triggering, significantly reduces the background fluorescence compared to using a continuous wave laser.

A schematic representation of the experimental setup is displayed in Fig. 3.1. It shows the laser beam, originating from the Nd:YAG laser, being expanded and collimated using lenses L_1 and L_2 and then reflected towards the heating cell using mirror M_1. BD_1 is a manually controlled beam dump, used to block the laser beam for shorter amounts of time, e.g., while inserting a sample into the cell. WP_1 is a waveplate, used to change the polarization of the laser beam, thereby changing the Raman signal emission direction, so that the background can be recorded while performing a measurement. The laser beam then reaches M_2, which is an arrangement of two mirrors used to change the height of the beam, to accommodate to the height of the cell. Lens L_3 is then used to send the beam into the cell in an angle while simultaneously focusing it in the middle of the cell. After exiting the cell, the beam is recollimated, and the propagation angle is changed

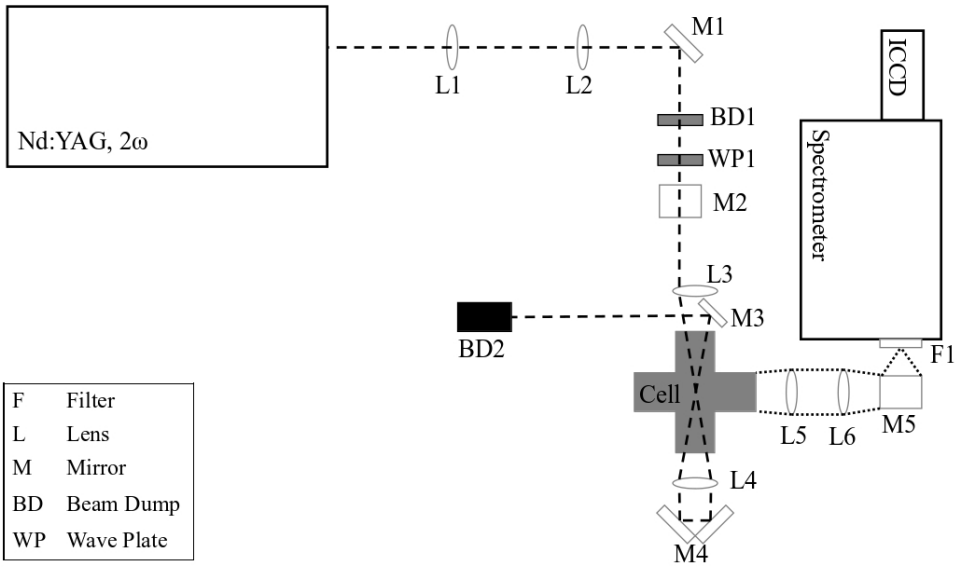

Figure 3.1: *Schematic representation of the experimental setup. The laser beam is collimated and guided towards the heating cell using an arrangement of lenses and mirrors. It is then focused in the center of the cell, where it makes a double-pass through the detection area and is then terminated in a beam dump. The Raman signal is focused onto the spectrometer entrance slit using a set of two lenses and an arrangement of mirrors.*

again using lens L_4. The mirror arrangement M_4 then directs the beam back into the cell, through lens L_4, thus enabling a double-pass measurement, which increases signal strength. Mirror M_3 then directs the beam into the water-cooled beam dump BD_2.

The Raman signal is collected at an angle perpendicular to that of the laser beam. Lens L_5 collects and collimates the signal and lens L_6 ($F_\# = 4$, cf. $F_\#$ 4.6 for the spectrometer) focuses the signal onto the slit of the spectrometer. M_5 is an arrangement of mirrors used to turn the image rotation and lower the beam, to accommodate to the height of the spectrometer slit, and F_1 is a Semrock EdgeBasic BLP01-532R-25 long-pass filter with OD_{abs} >6 at 532 nm, used to block any scattered light from the laser.

The spectrometer used for the measurements is a Princeton Instruments IsoPlane SCT-320 grating spectrometer with a rotating grating selector - employing one grating of density 600 g/mm, blazed at 500 nm (the one used during measurements), and one grating of density 1800 g/mm, also blazed at 500 nm - and a manually controlled entrance slit, set to 250 μm. At the exit of the spectrometer a Princeton Instruments PI-MAX 4 ICCD camera with chip size 1024x256 pixels (pixel size 26x26 μm) is mounted. The camera intensifier is triggered by the laser pulse generator, with the gate width set to 25 ns in order to suppress continuous background light while also transmitting the entire, momentary, laser-induced Raman signal. During measurements, an on-CCD accumulation value of 2000 shots and one exposure per frame were used in combination with a gain

value of 20 and binning of 150 pixels in vertical direction.

3.2 Heating cell

The cell itself consists of a cruciform aluminum pipe with the option to mount windows at each end, see Fig. 3.2a. Three of the ends - the two along the propagation direction of the laser beam and the one in the direction of signal collection - are fitted with windows while the fourth one is kept intentionally open. This allows for a way to insert the sample and a thermocouple for temperature measurements, while also providing an outlet for the gas formed during the heating process.

To remove air from inside of the pipe, it is flushed with Ar from three gas inlets. Two of the inlets are located on top of the pipe at the ends along the laser beam propagation direction while the third is added as an attachment between the pipe opening and the window in the direction of the signal collection. The flow of Ar is controlled using a rotameter, which is also used to mix the Ar with O_2 during the gasification measurements. During pyrolysis the rotameter was set to a flow rate of 4.2 l/min for Ar, and during gasification it was set to 4.0 l/min for Ar and 0.167 l/min for O_2, resulting in an O_2 concentration of 4% (equivalent to 20% of the O_2 concentration in ambient air).

A 3 m long heating wire from Hemi Heating, able to reach a temperature of approximately 670 K, according to documentation, is wrapped around the cell and connected to a transformer. The cell is then insulated by a layer of glass fiber wool between two layers of aluminum foil, to improve the heating efficiency of the wire. The insulated cell can be seen in Fig. 3.2b, and with this setup, the center of the cell reaches a temperature of approximately 770 K, at a rate of approximately 38 K/min.

3.3 Samples

Measurements were performed on seven different biomass samples, one provided from Research Institute of Sweden (RISE), Borås, and six from Vattenfall Research and Development. The samples, along with the masses used during measurements, are listed in Tab. 3.1, and photos of the samples are provided in Figs. 3.3-3.4. Specifications on composition are, at this stage, only available for samples 1 [16] and 7 [17]. These are listed in Tabs. 3.2-3.3.

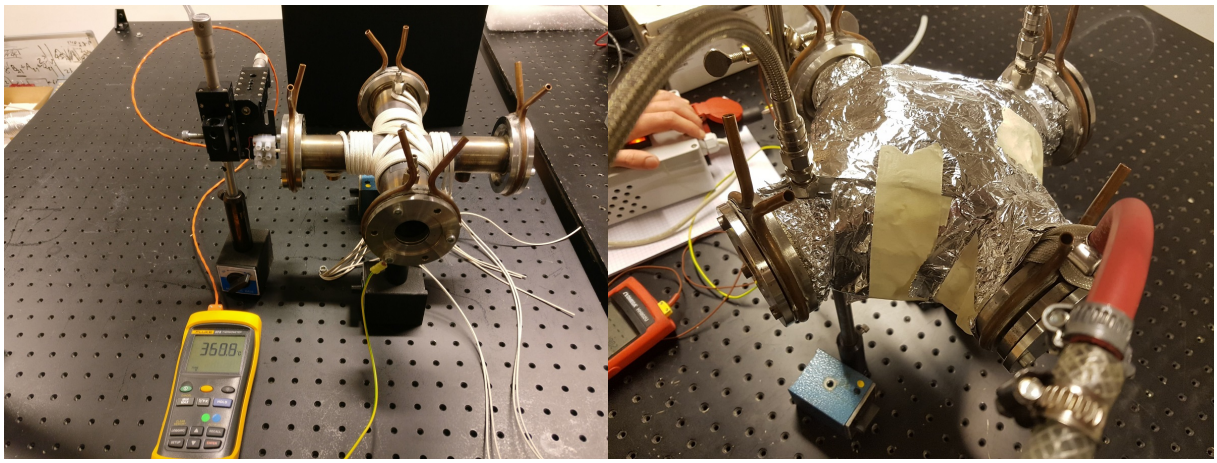

(a) (b)

Figure 3.2: *Photos of the heating cell, showing (a) the heating cell during initial heating trials and (b) the heating cell setup used during measurements. With the setup in (a), an inner temperature of ∼630 K is reached while the setup displayed in (b) reaches an inner temperature of ∼770 K.*

Table 3.1: *List of the samples featured in the measurements, showing supplier, identifier code, mass, and figure reference.*

Sample no.	Supplier	Identifier	Mass	Fig.
1	RISE	Wood pellet	2.440 g	3.3
2	Vattenfall	BP BD 212	2.071 g	3.4a
3	Vattenfall	BP BD 233	2.534 g	3.4b
4	Vattenfall	BP BD 166	2.057 g	3.4c
5	Vattenfall	BP BD 145	1.315 g	3.4d
6	Vattenfall	BP BD 139	2.725 g	3.4e
7	Vattenfall	Dixie	1.566 g	3.4f

Table 3.2: *Specifications of Sample 1 [16]. Components with concentrations <0.01 mass-% purposely omitted.*

Parameter	Unit	Value	Parameter	Unit	Value
moisture content	(mass-%)	0.4	O	(mass-%, dry)	43
combustible part	(mass-%, dry)	99.6	N	(mass-%, dry)	0.08
ash part	(mass-%, dry)	0.4	K	(mass-%, dry)	0.05
C	(mass-%, dry)	50.7	Ca	(mass-%, dry)	0.1
H	(mass-%, dry)	6.2	Si	(mass-%, dry)	0.02

Table 3.3: *Specifications of Sample 7 [17]. Components with concentrations <0.01 mass-% purposely omitted.*

Parameter	Unit	Value	Parameter	Unit	Value
moisture content	(mass-%)	<10	N	(mass-%, dry)	<0.2
combustible part	(mass-%, dry)	70-90	Cl	(mass-%, dry)	<0.3
ash part	(mass-%, dry)	<3	S	(mass-%, dry)	<0.2
C	(mass-%, dry)	40-55	Cu	(mass-%, dry)	<0.02
H	(mass-%, dry)	5-8	Pb	(mass-%, dry)	<0.02
O	(mass-%, dry)	40-50	Fl	(mass-%, dry)	<0.03

3.4 Measurement procedure

3.4.1 Pyrolysis

Before starting the flow of Ar, the Raman signal in ambient air was measured to use for normalization during the data processing. The beam was then blocked, using BD_1, and the sample - placed on a small tray constructed out of copper wire and aluminum foil - was inserted into the center of the heating cell. Then, the beam was unblocked, the measurement sequence was started, and the heating was switched on, heating the cell from room temperature (∼300 K) to ∼770 K. During heating, the temperature was periodically noted, later to be used for data analysis. When no signal was longer visible, the sequence was ended, and the sample was removed. A new sample was then placed into the cell - in the exact same way as for the previous measurement sequence - to measure the signal during rapid heating, which was used to compare the differences between the two processes.

During measurements, the background fluorescence was measured at multiple points in time. This was done by rotating the polarization of the incident laser beam 90° using

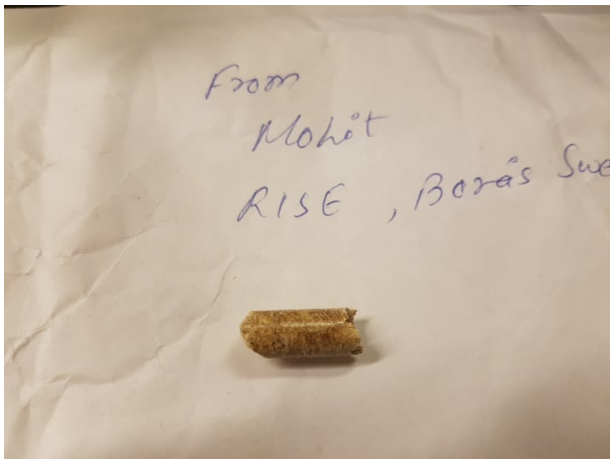

Figure 3.3: *Picture of the wood pellet provided by RISE (listed in Tab 3.1).*

(a) (b)

(c) (d)

(e) (f)

Figure 3.4: *Pictures of the samples provided by Vattenfall Research and Development (listed in Tab 3.1), showing (a) the Vattenfall BP BD 212, (b) the Vattenfall BP BD 233, (c) the Vattenfall BP BD 166, (d) the Vattenfall BP BD 145, (e) the Vattenfall BP BD 139, and (f) the Vattenfall Dixie.*

waveplate WP_1 - described in Section 3.1 - thereby allowing a simple way to discriminate the background fluorescence from the Raman signal in the data post-processing.

3.4.2 Gasification

For gasification, the process was largely similar to that of the pyrolysis measurement sequence, the difference being that two additional background measurements were performed before the heating was switched on, to be used during the data analysis. The first one of these was after the flow of Ar and O_2 was started, and the second one was after inserting the sample into the cell, right before the start of the main sequence.

3.5 Data processing

As the major downside to RS is known to be the low signal-to-noise ratio (SNR), a lot of post-processing of the acquired data is needed in order to present significant interpretations of the results. First, the data were averaged over 20 consecutive frames, to reduce noise and allow any peaks to be easier distinguished. Then, a combination of a linear interpolation and a second-degree polynomial fitting was applied to the background, which was subsequently subtracted. This process is presented in Fig. 3.5. Fig. 3.5a shows the raw, recorded spectrum from the gasification measurement of Sample 7. In Fig. 3.5b, the same spectrum is shown together with the fitted background, where the left part (565-590 nm) is fitted using linear interpolation and the right part (590-642 nm) is fitted using a second-degree polynomial function. The reason for doing this is that using only a polynomial fitting method resulted in unrealistic shapes for the left part of the spectrum. The result of subtracting this fitted background is then presented in Fig. 3.5c.

For preparation of the temperature versus concentration plots, interpolation was used to subtract the remaining background from the peaks, which were then normalized versus the N_2 peak from the frames recorded in ambient air, as a way to determine the species concentration. The temperature scale was calculated by applying a second-degree polynomial fitting to the temperatures noted for the different frames during the measurement sequences, as the change in temperature over time was not entirely linear. This temperature was also used to make 2D images, showing how the signal intensity at different wavelengths changes with increasing temperature.

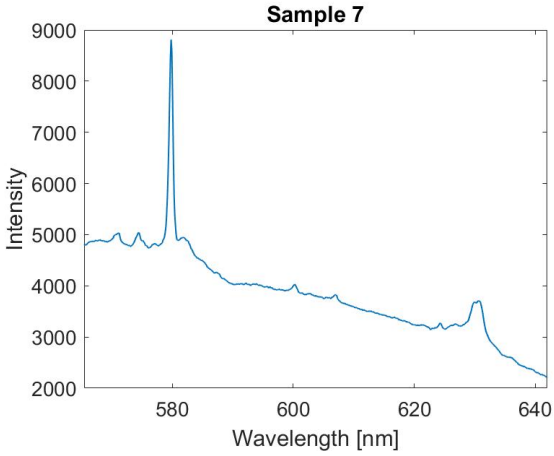

(a)

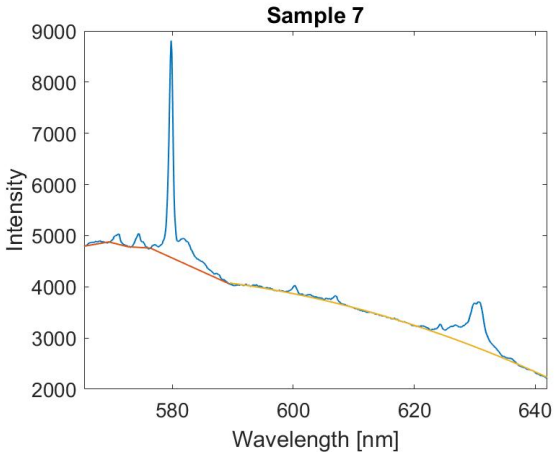

(b)

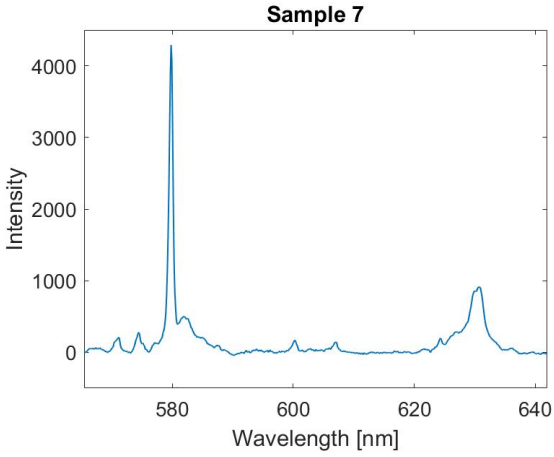

(c)

Figure 3.5: *Recorded spectrum from the gasification measurement of Sample 7, showing the same spectrum (a) pre-processing, (b) with split-fitting of the background using linear interpolation and a second-degree polynomial fitting, and (c) the resulting spectrum.*

Chapter 4

Results & Discussion

4.1 Pyrolysis

A 2D image from the measurement sequence of Sample 7 is presented in Fig. 4.1a, which shows the recorded signal as wavelengths versus temperature. At the start of the measurement at room temperature, lines are visible in the lower part of the image, at wavelengths 607 nm, 652 nm, and 660 nm, together with some background fluorescence, spread evenly over the spectral range. These lines correspond to the vibrational frequencies 2331 cm^{-1} of N_2, 3460 cm^{-1} of the -NH_2 group, and the 3657 cm^{-1} asymmetric stretch of H_2O, respectively. As the cell reaches a temperature of ∼500 K, the N_2 and -NH_2 lines vanish, and a new line appears at 630 nm. This line corresponds to vibrational frequency 2924 cm^{-1}, which is close both to the asymmetric stretch of the -CH_3 group and the asymmetric stretch of the -CH_2- group. There is also a very faint line visible at ∼657 nm, which corresponds to the vibrational frequency 3600 cm^{-1} of some -OH group. The images of samples 3, 5 and 6 (Figs. 4.2c, 4.2e, and 4.2f) show similar trends, while in the images of samples 1, 2 and 4 (Figs. 4.2a, 4.2b, and 4.2d), there seems to be no sign of the initial N_2 and -NH_2 lines.

Fig 4.1b shows an averaged spectrum of the recorded signal of Sample 7, where the detected species are marked using dashed lines. It shows a broad peak between wavelengths 623 nm and 635 nm, centered around 630 nm, resulting from a superposition of signals from different hydrocarbon compounds with vibrational frequencies of 2746-3049 cm^{-1}, where 630 nm roughly corresponds to the strong vibrational frequency 2930 cm^{-1} of the asymmetric stretch of the -CH_2- bond. The small peak of the -NH_2 group is visible at 652 nm, corresponding to the vibrational frequency 3460 cm^{-1}. According to tabulated values, NH_3 has degenerate symmetric and anti-symmetric stretching with strong signals in this area and has been observed earlier, during similar experiments, thus making its presence highly plausible [9, 13, 18]. The NH_3 would most likely originate from NH_4^+, which trees absorb from the soil via the roots, and use to synthesize proteins [19, 20].

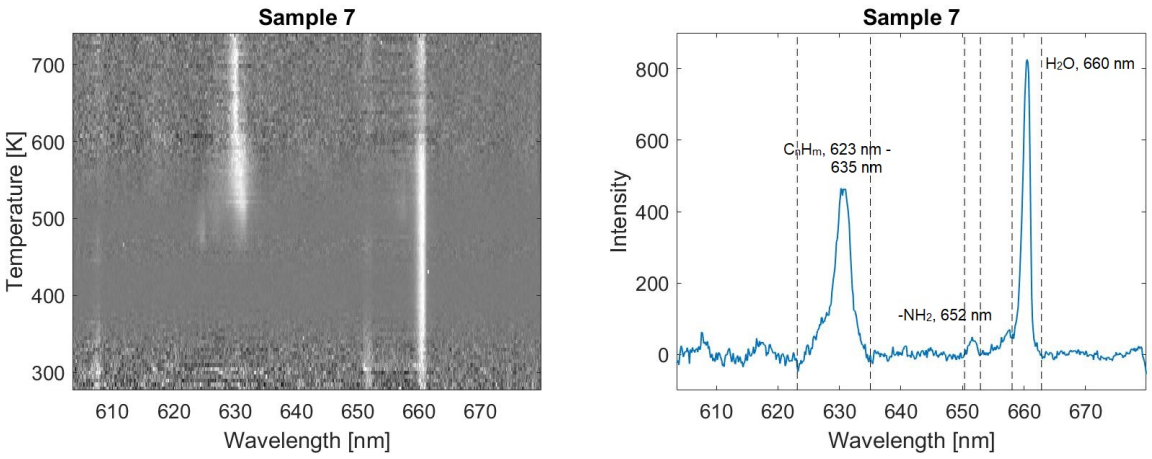

(a) (b)

Figure 4.1: *In (a), a 2D image of the measurement sequence of Sample 7 can be seen, showing how the recorded intensity changes with increasing temperature for different wavelengths, and in (b) the recorded spectrum of the same sample, averaged over the whole measurement sequence, is displayed. The marked regions show different CH-species between wavelengths 623 nm and 635 nm, -NH_2 at 652 nm, and H_2O at 660 nm.*

The concentration of NH_4^+ is often higher in the bark than in the wood, which would suggest that the samples containing these traces contains a higher amount of bark than the others [21]. This coincides with that the traces were found in samples 2, 3, 5, 6, and 7, which all - Sample 7 being an exception - have a dark brown color (see Figs. 3.4a, 3.4b, 3.4d, 3.4e, and 3.4f in Section 3.3), suggesting they are made from bark. However, the concentration of the -NH_2 group was too low to be able to evaluate and present a satisfactory concentration plot of the species. The strong peak visible at 660 nm - as mentioned earlier - corresponds to the asymmetric stretch of H_2O, with vibrational frequency 3657 cm^{-1}.

While the spectra appear rather similar for all seven samples, there are some differences, the major one being the presence of N_2 and -NH_2 groups at temperatures below 500 K for samples 2, 3, 5, 6, and 7. Minor differences can also be seen in the hydrocarbon region, e.g., the width of the region is different for the different samples, and in the 2D images more than one line can sometimes be seen, but the low resolution ($\sim$8 cm^{-1}, limited by the grating density and spectrometer entrance slit width) makes it hard to draw any conclusions related to this observation. An example of a spectrum where one of these extra CH group lines can be seen is presented in Fig. 4.3, along with the previously mentioned -OH group lines. The figure shows a spectrum of Sample 7, averaged over 20 frames, around 500 K. The marked area between 623 nm and 625 nm shows a peak from a CH group, centered around 625 nm, which corresponds to a vibrational frequency of 2794 cm^{-1}, and the marked area between 656 nm and 658 nm shows the -OH group peak, centered around 657 nm, corresponding to a vibrational frequency of 3576 cm^{-1}, which could correspond to some kind of aldehyde (e.g. formaldehyde) [23].

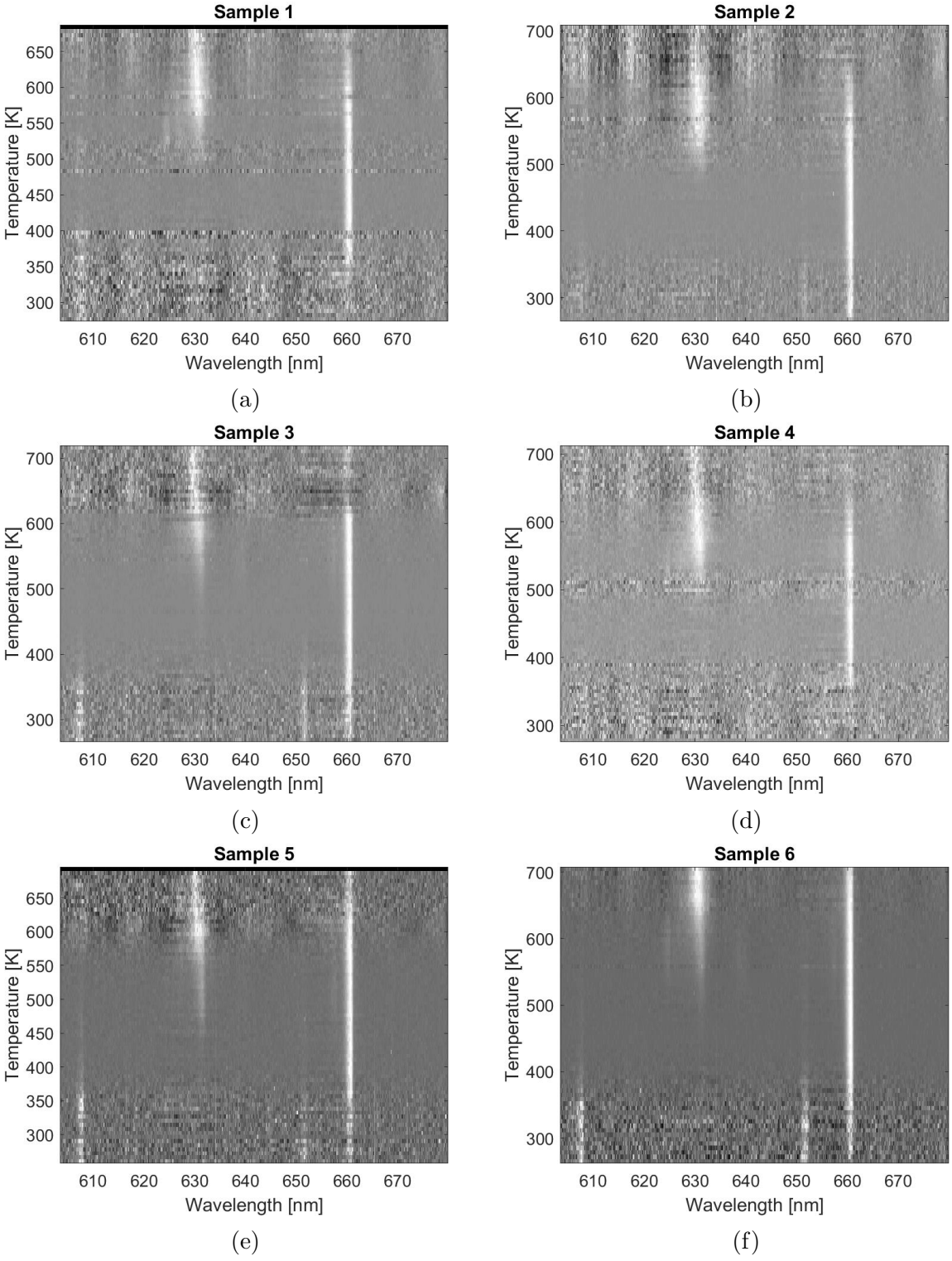

Figure 4.2: *2D images of the measurement sequence of (a) Sample 1, (b) Sample 2, (c) Sample 3, (d) Sample 4, (e) Sample 5, and (f) Sample 6, showing how the recorded intensity changes with increasing temperature for different wavelengths.*

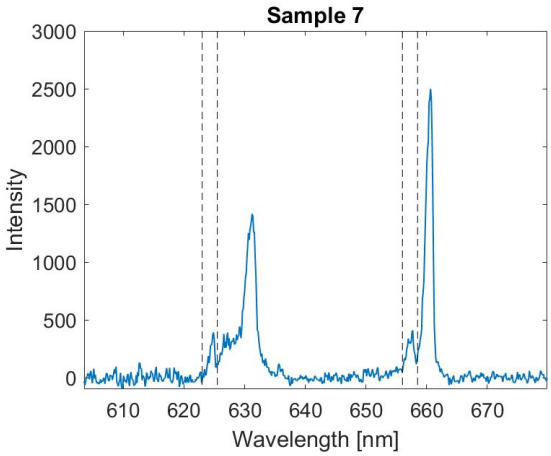

Figure 4.3: *Spectrum of Sample 7, averaged over 20 frames, around 500 K. The marked region between 623 nm and 625 nm shows a peak from a CH group, centered around 625 nm, and the marked region between 656 nm and 658 nm shows the -OH group peak, centered around 657 nm.*

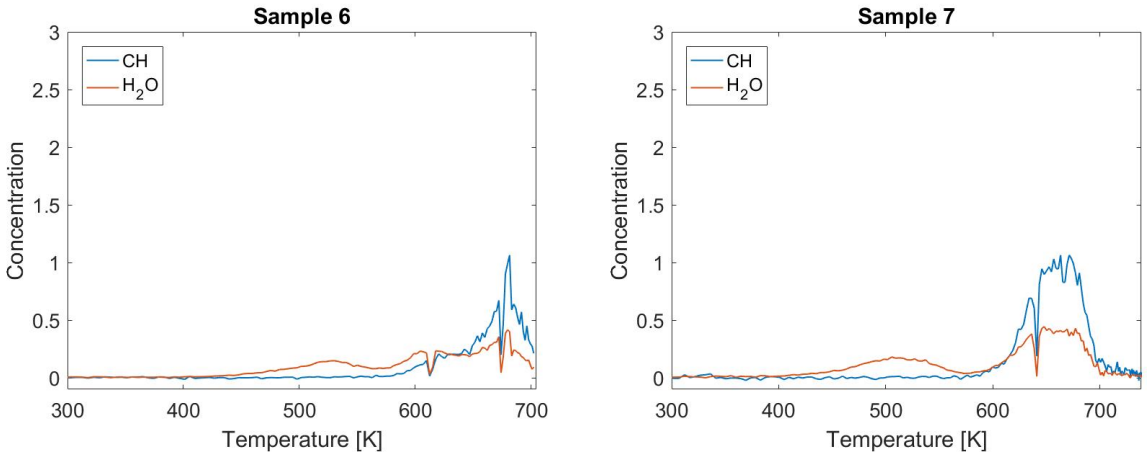

(a) (b)

Figure 4.4: *H_2O concentration versus temperature for (a) Sample 6 and (b) Sample 7, with CH concentration added for comparison.*

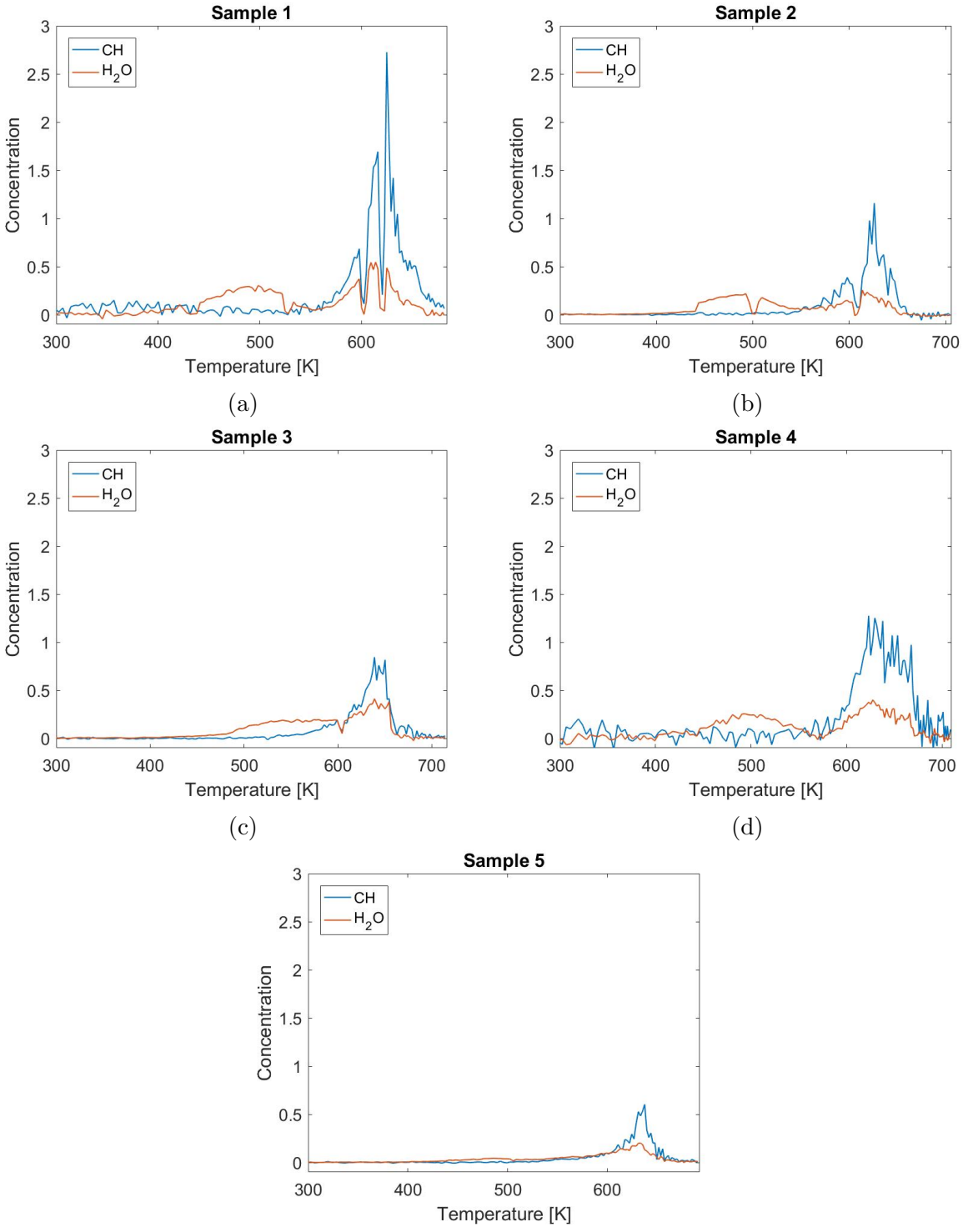

Figure 4.5: *H_2O concentration versus temperature for (a) Sample 1, (b) Sample 2, (c) Sample 3, (d) Sample 4, and (e) Sample 5, with CH concentration added for comparison.*

Figs. 4.4a and 4.4b show how the H_2O concentration changes for samples 6 and 7 as the temperature increases, with the concentration evaluated for the CH region added for comparison (similar plots for the other samples can be seen in Fig. 4.5). In Fig. 4.4a, the H_2O concentration first starts to increase at ∼425 K, reaching a peak at ∼525 K. It then decreases and increases again, reaching a peak at ∼610 K, and then decreases slightly before reaching its final peak at ∼675 K. The CH concentration level lies stable at zero until it starts increasing at ∼575 K, reaching its peak value at ∼675 K. Fig. 4.4b shows a similar pattern, where the H_2O concentration starts increasing at ∼425 K, reaching a peak at ∼510 K, then decreasing and increasing again, reaching its second and final peak at ∼650 K. This behavior is similar for the other samples, shown in Fig. 4.5. The sharp dips located at ∼610 K and ∼675 K in Fig. 4.4a and at ∼640 K in Fig. 4.4b are due to changing the polarization of the laser in order to measure the background. Furthermore, the fact that these dips reach zero indicates that the method of background subtraction used, works.

An explanation of this cyclic behavior of the H_2O is that the first peak corresponds to the evaporation of moisture from the surface of the sample - commonly referred to as the evaporation phase - and as the surface then starts to dry out, the concentration decreases. When the surface then turns into char, moisture in the form of H_2O and tar (*bio-oil*, as defined in Section 1.1.1), starts evaporating from the bulk material, which results in the second peak. Due to the lack of information about the provided samples it is, at this stage, hard to explain why Sample 6 has three cycles of water evaporation. One simple explanation could be that the thickness of the sample results in one evaporation phase from the surface and two phases for the outer and inner part of the bulk material.

Figs. 4.6a and 4.6b show two cases of CH and tar signal as a function of increasing temperature, for samples 1 and 5, respectively (the same plots for the other samples can be seen in Fig. 4.7). In Fig. 4.6a, the CH concentration lies around zero up until ∼575 K, where it starts increasing until it reaches its peak at ∼625 K, from which it then rapidly decreases. As previously mentioned, the two dips in the concentration spectrum, located at 600 K and 620 K, are due to changing the polarization of the laser in order to measure the background. What is labeled as tar signal is actually the recorded fluorescence background of the spectra, and observing the spectrum for Sample 1, some fluorescence can be seen at low temperatures when tars cannot possible be emitted from the sample. Here (as well as for Sample 4, in Fig. 4.7c), the fluorescence instead originates from the lightly colored and shiny surface of the sample. This fluorescence then decreases as the surface darkens and turns to charcoal, with a minimum at ∼590 K. Subsequently, the fluorescence starts to rapidly increase, reaching a peak at ∼625 K, together with the CH peak, before it rapidly decreases. This peak is due to the fluorescence emitted from the tar and heavy hydrocarbons released from the sample in this temperature range. In Fig. 4.6b, both the CH concentration and the fluorescence

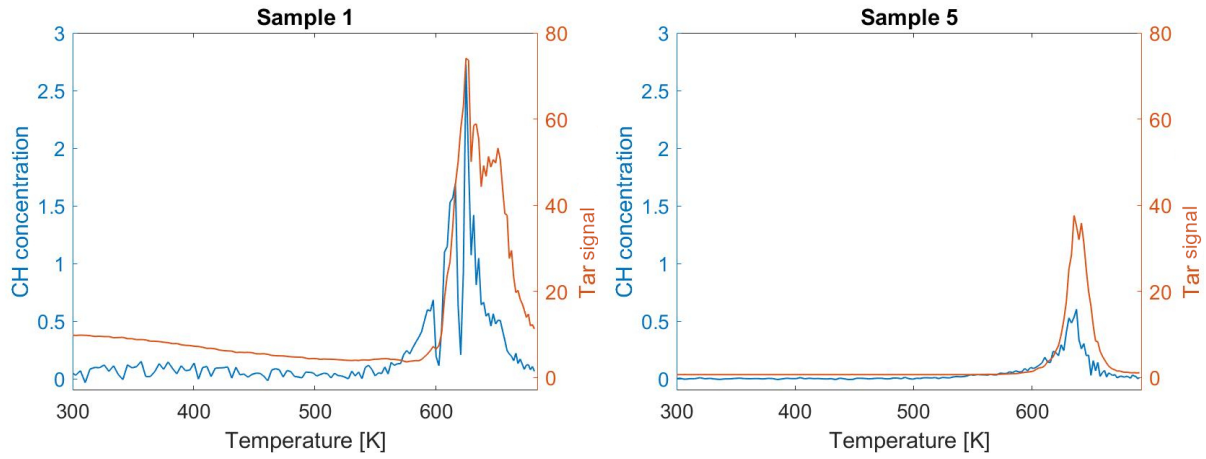

Figure 4.6: *CH concentrations and tar signals, emitted from (a) Sample 1 and (b Sample 5, as a function of temperature.*

start at zero. The CH concentration starts increasing at ∼540 K, reaching a peak at ∼630 K, then starts decreasing rapidly. The fluorescence starts increasing at ∼590 K, reaches its peak at ∼640 K, and then decreases rapidly.

For Sample 1 (Fig. 4.6a), it can quite clearly be seen that the emission of CH starts at lower temperatures than the emission of tar. This is not true for all samples though, as for some the emission of the two are rather simultaneous. Compared to Sample 5 (Fig. 4.6b), Sample 1 also emits much larger amounts of both CH and tar. The interesting thing about Sample 5 is that the emission process appears to occur within a narrower temperature range (and therefore under a shorter amount of time, since the heating rate was similar for all the measured cases). It can be speculated that this is due to the sample being more compact than the other samples and having a larger surface to bulk ratio.

The results from the pyrolysis measurements were what was to be expected. Since the sample is heated up in an inert environment, few reactions take place, and most of the signals therefore originates from species emitted directly from the sample. As seen in Tab. 3.2, after drying, the samples consist mostly of the elements C, O, H, and N. The expected species to find are therefore: H_2O, hydrocarbons (e.g. aldehydes, ketones, and phenols), and possibly traces of nitrogen compounds (NH_2) [16].

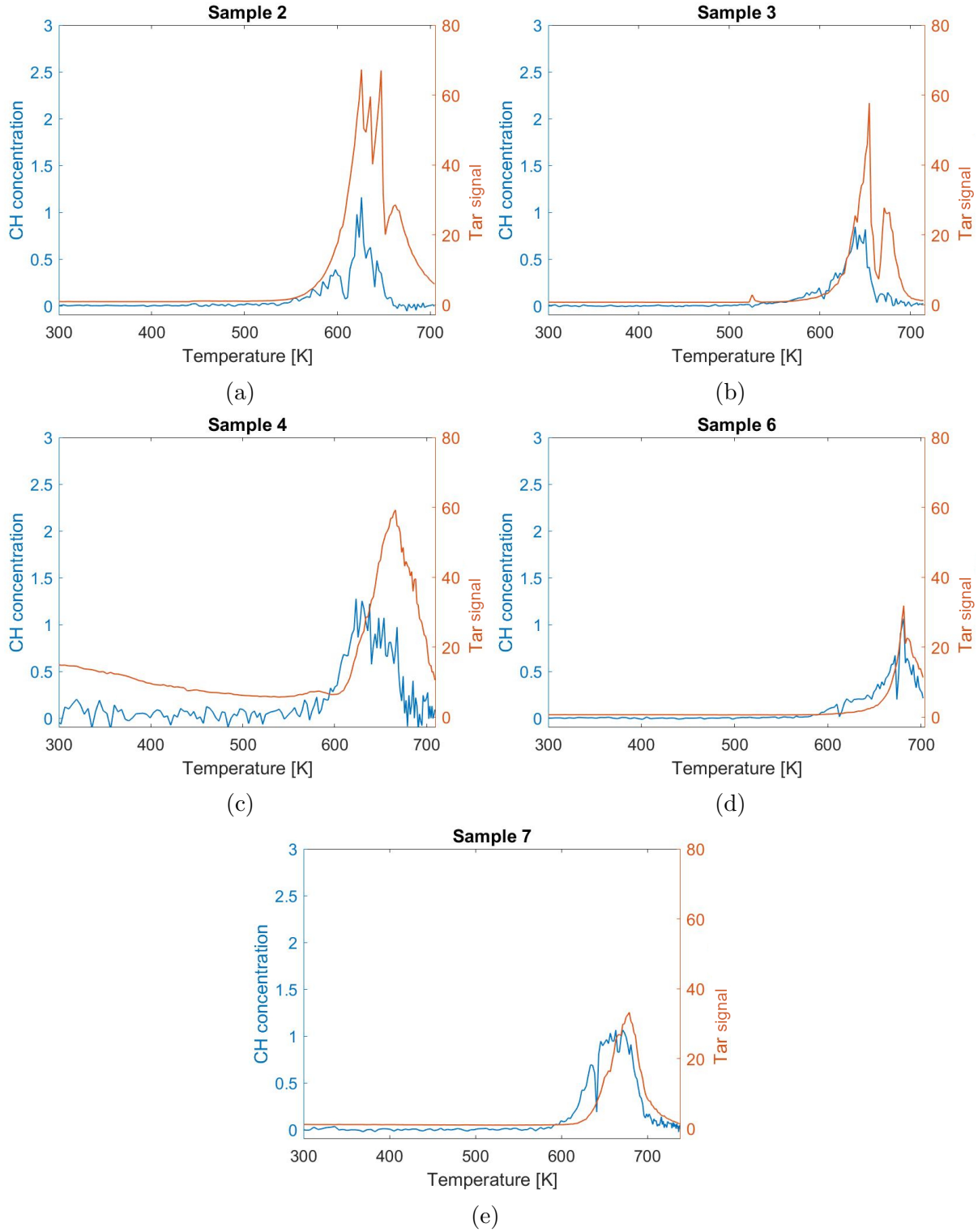

Figure 4.7: *CH concentrations and tar signals, emitted from (a) Sample 2, (b) Sample 3, (c) Sample 4, (d) Sample 6, and (e) Sample 7, as a function of temperature.*

4.2 Gasification

Traces of several species were observed during the gasification measurements. Fig. 4.8a shows a 2D image representation of how the recorded signal intensities at different wavelengths changed with increasing temperature for Sample 7 (the 2D images of the other samples are displayed in Fig. 4.9). Here, a strong line is visible at ∼580 nm, ranging from the start of the sequence to the end. This line corresponds to a vibrational frequency of 1556 cm^{-1}, and originates from the O_2 that was added to the cell. A faint line, stretching from start to finish, can also be seen at 607 nm, corresponding to a vibrational frequency of 2323 cm^{-1}, originating from residual traces of N_2 in the cell. At 450 K, several lines start appearing. The two lines located at 571 nm and 574 nm correspond to the vibrational frequencies 1285 cm^{-1} and 1388 cm^{-1} of the symmetric stretching of the CO_2 molecule. A few lines also appear between wavelengths 578 nm and 586 nm. These lines correspond to vibrational frequencies in the range 1496-1768 cm^{-1}, which is where stretching vibrations of the >C=O group occur. Around wavelengths 620-640 nm another cluster of lines is visible, corresponding to the vibrational frequency range 2668-3172 cm^{-1}. This is known as the CH-stretch region, since it covers the vibrational frequencies of multiple types of CH groups, with the strongest one being the asymmetric stretch of the -CH_2- group, at 2930 cm^{-1} (∼630 nm), as previously discussed in Section 4.1. Between 500 K and 550 K, the image is dominated by background fluorescence, and after it has decreased, all the >C=O group lines and most of the CH group lines have disappeared. At 550 K, another line emerges at 600 nm, corresponding to the vibrational frequency 2130 cm^{-1}, which originates from CO.

Fig. 4.8b shows the recorded spectrum, averaged over all the recorded frames, with the peaks of the different species and their respective wavelengths marked. The two small leftmost peaks at 571 nm and 574 nm corresponds to the vibrational frequencies 1285 cm^{-1} and 1388 cm^{-1} of the symmetric stretching of CO_2. O_2 can be seen at 580 nm (vibrational frequency 2323 cm^{-1}), directly followed by the >C=O stretch between 580 nm and 590 nm, corresponding to vibrational frequencies 1496-1768 cm^{-1}. At 600 nm (2130 cm^{-1}) the small CO peak is visible, adjacent to the residual N_2 peak at 607 nm (2323 cm^{-1}). The right part of the spectrum is dominated by the CH stretch between wavelengths 620 nm and 640 nm, corresponding to vibrational frequencies of 2668-3172 cm^{-1}, with the highest point located at 630 nm (2930 cm^{-1}), representing the asymmetric stretch of the -CH_2- group.

As can be seen in Fig. 4.8a, the peaks in the >C=O stretch and the peaks in the CH stretch start appearing around the same temperature mark (450 K). The fact that these two kinds of vibration occur simultaneously, strongly suggest that the partial oxidation leads to the formation of different aldehydes - with the structure RCHO, where R is some CH group - and ketones - with the structure RC(=O)R', where both R and R' are various

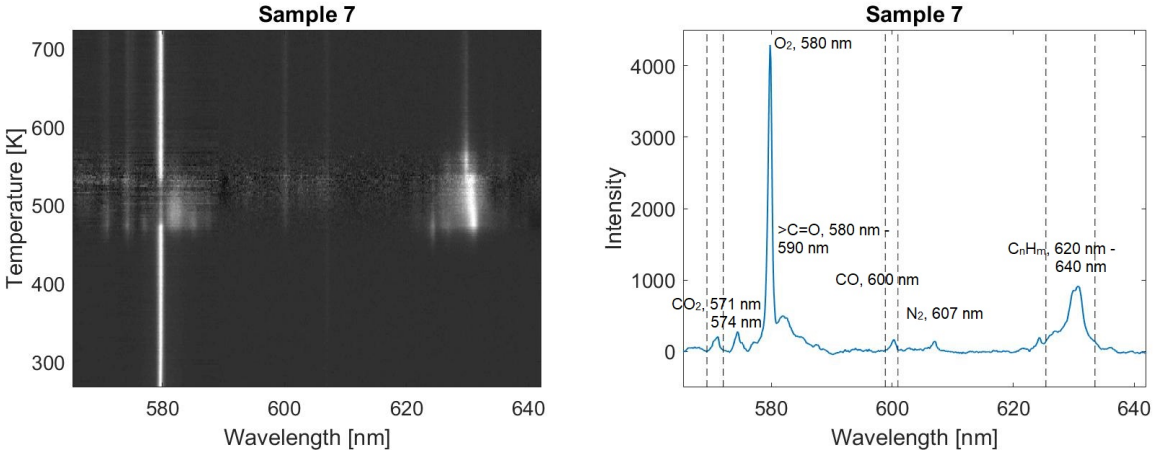

(a) (b)

Figure 4.8: *In (a), a 2D image of the measurement sequence of Sample 7 can be seen, showing how the recorded intensity changes with increasing temperature for different wavelengths, and in (b) the recorded spectrum of the same sample, averaged over the whole measurement sequence, is displayed. The marked regions show CO_2 at 571 nm and 574 nm, O_2 at 580 nm, different >C=O groups between 580 nm and 590 nm, CO at 600 nm, residual traces of N_2 at 607 nm, and different CH groups between wavelengths 620 nm and 640 nm.*

kinds of CH groups - such as formaldehyde, acetaldehyde, and acetone, which are known to emit strong Raman signals at these wavelengths [18]. This is also consistent with what has been found in previous studies on pyrolysis and gasification [22, 23, 24]. As expected for a partial oxidation process, CO and CO_2 are also formed. In contrast to combustion, CO_2, which is usually formed after CO, here appears to start forming around 450 K - simultaneously with the >C=O peaks - while CO starts appearing first around 550 K. The formation of CO and CO_2 is a balanced reaction,

$$CO + \frac{1}{2}O_2 \rightleftharpoons CO_2,$$

determined by temperature and the availability of O_2. One reason for the observed behavior could then be that the O_2 concentration starts out at a high level, leading to all of the formed CO immediately reacting to form CO_2. The O_2 level then decreases, until a balance is reached between the formation of CO and CO_2.

Fig. 4.10 shows how the concentration of CO_2 changes with increasing temperature, compared to the CH concentration, for all the measured samples. The following discussion focuses on samples 1 and 5 (Figs. 4.10a and 4.10d), but similar trends can be seen in the other samples as well.

In Fig. 4.10a, the CH concentration is zero until ∼550 K, where it starts increasing until it reaches a peak at ∼650 K. From here, it then decreases to a value slightly above zero. CO_2 behaves in a similar manner but starts increasing first at ∼580 K, then reaches a peak at ∼640 K before immediately decreasing to a value slightly above zero. Given

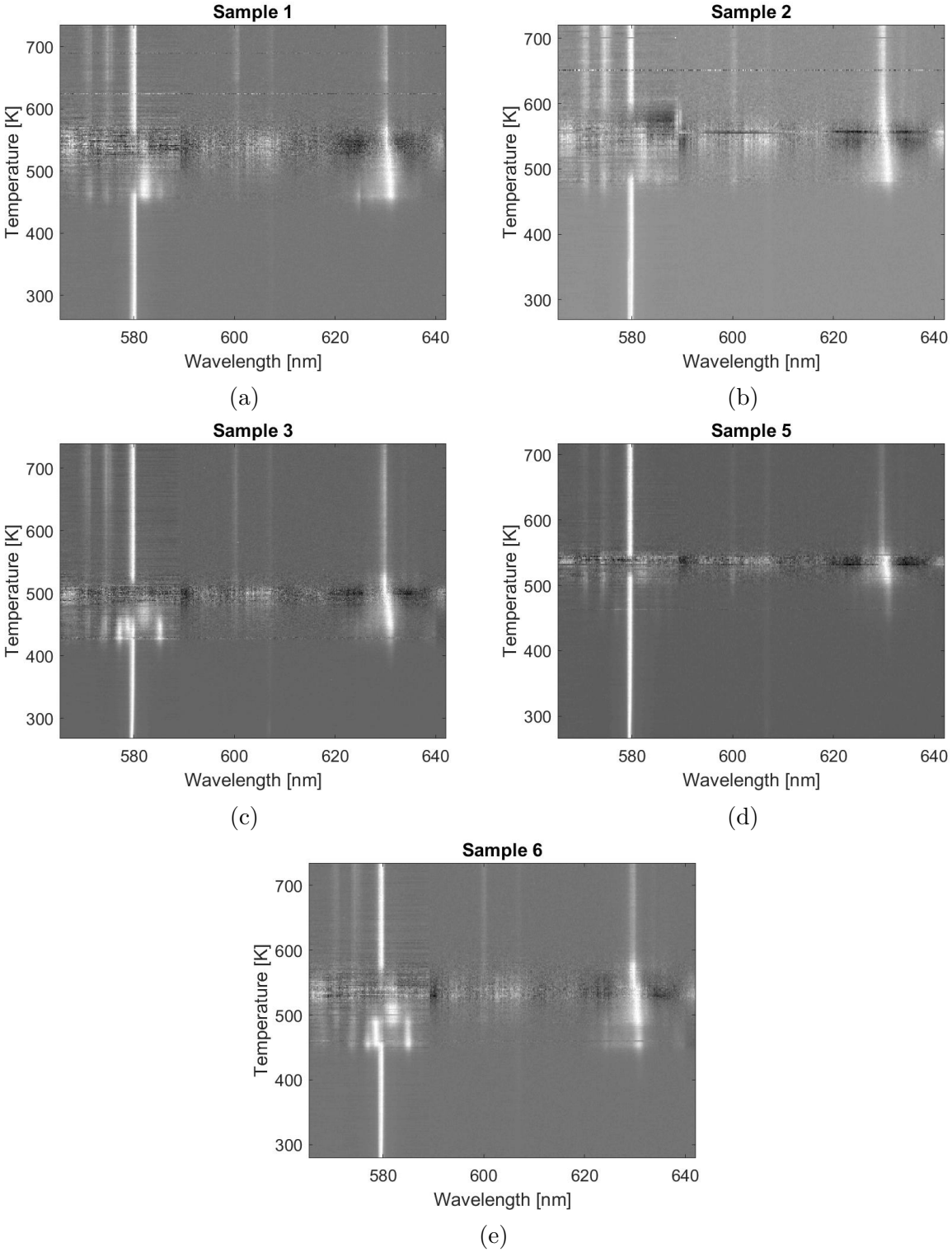

Figure 4.9: *2D image of the measurement sequence of (a) Sample 1, (b) Sample 2, (c) Sample 3, (d) Sample 5, and (e) Sample 6, showing how the recorded intensity changes with increasing temperature for different wavelengths.*

enough time for the cell to ventilate, it will most certainly, eventually, decrease completely to zero.

Fig. 4.10d shows a similar behavior, but here the concentrations for both CO_2 and CH are significantly lower. Both the CO_2 and CH is zero until ∼525 K, where they start to increase, reaching a peak at ∼600 K, before decreasing and stabilizing at a close-to-zero level.

Fig. 4.11 shows how the CO concentration changes with the increasing temperature, compared to the concentration of CH, for all the measured samples. The following discussion focuses on samples 1 and 7 (Figs. 4.11a and 4.11f).

In Fig. 4.11a, the CO concentration is close to zero until ∼600 K, where it starts to increase until reaching a peak at ∼650 K, before it slowly decreases to a value slightly above zero. This can be compared to the CH concentration, which starts increasing from zero at ∼550 K, reaches a peak at ∼650 K, before it rapidly decreases towards a value of zero.

In Fig. 4.11f, the CO concentration starts to increase at a temperature ∼560 K and reaches a peak at ∼600 K, before it slowly decreases to a value where it stabilizes just above a zero level. The CH concentration, on the other hand, starts to increase rapidly at ∼530 K, then also reaches a peak at ∼600 K and subsequently decreases towards a zero value.

It might appear as if the concentrations presented in Figs. 4.10-4.11 does not support the data presented in Fig. 4.9, where the lines representing CO_2 and CO seem to show a quite homogeneous behavior as the temperature increases, but, in the 550-600 K region of the image, a high increase of the intensity can be seen all over the wavelength range. This can also be attributed to that the lines are simply easier to distinguish when observed against the subtracted background fluorescence, than when viewed as concentration versus temperature.

As a way to quantify the results, the maximum relative concentration of each species was calculated for each sample. These are listed in Fig. 4.12. The cross sections used were taken from Tab. 5.1 in Eckbreth [12]. For the CH group species, the cross section used in the calculations was taken as an average of the cross sections for CH groups listed there. The concentration of the different species was taken from their peak value in the concentration versus temperature plots, since they coincide in all of the samples. In the table it can be seen that the gas produced from the different samples, at this point, mainly consists of different CH group species, with concentrations ranging from 49% to 64%, while CO_2 concentrations ranges from 21% to 29% and CO concentrations from 12% to 22%.

The results from the gasification measurements showed some quite interesting findings, although not previously entirely unheard of. The emission of CO and CO_2 was to be expected, as gasification is a partial oxidation process. What was not expected was that the emission of CO consistently seems to appear after the emission of CO_2, when it,

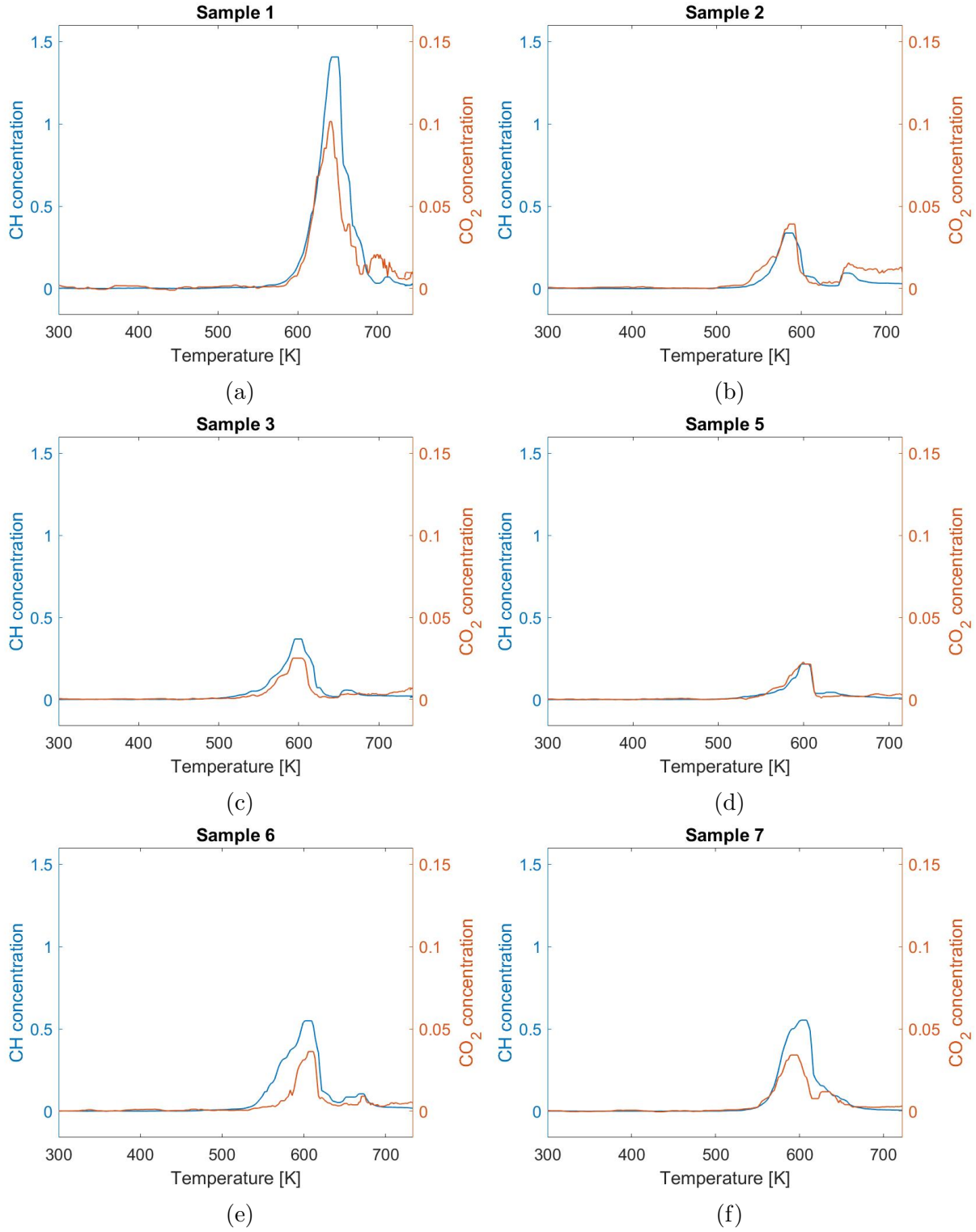

Figure 4.10: *CH and CO_2 concentrations, emitted from (a) Sample 1, (b) Sample 2, (c) Sample 3, (d) Sample 5, (e) Sample 6, and (f) Sample 7, as a function of temperature.*

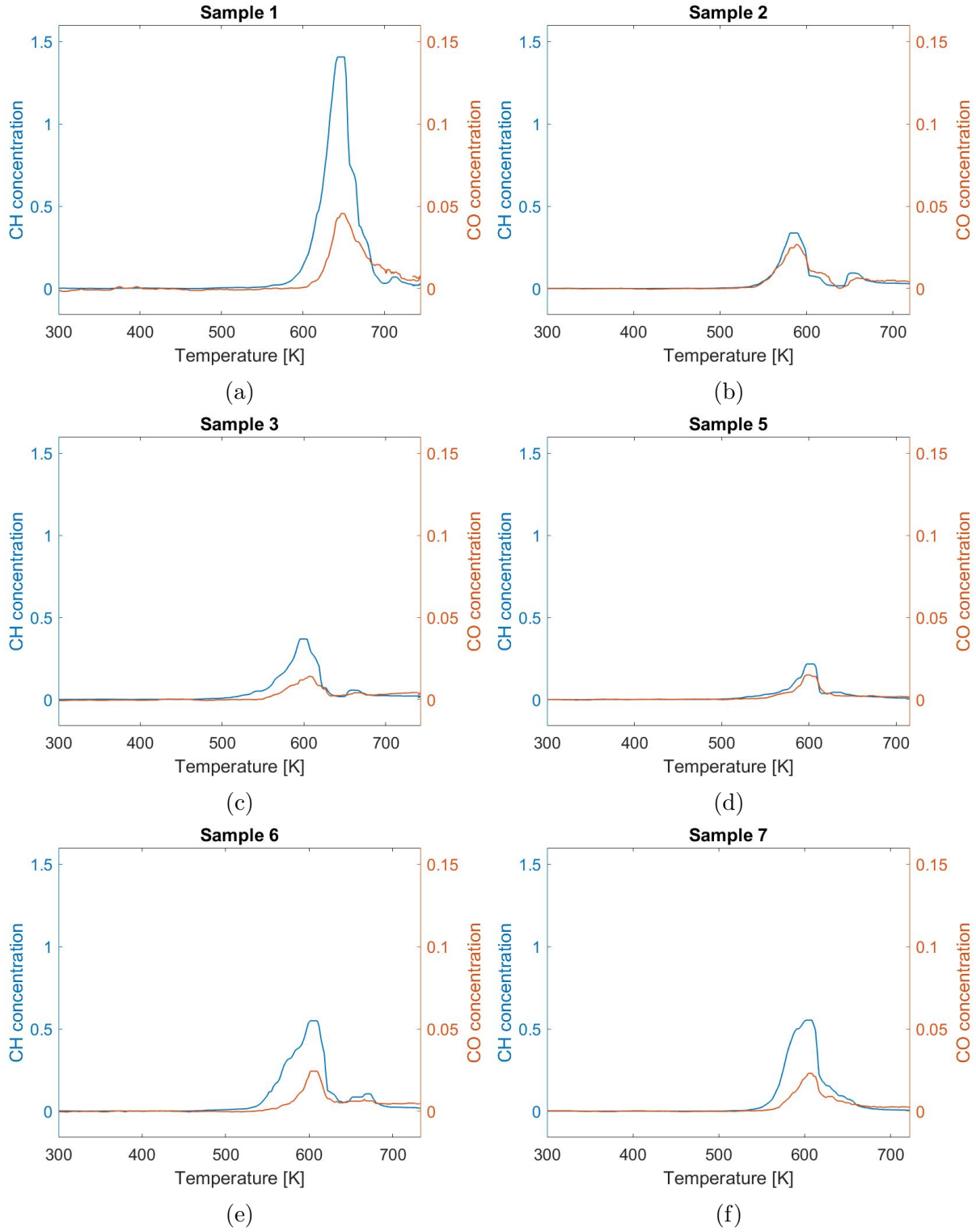

Figure 4.11: *CH and CO concentrations, emitted from (a) Sample 1, (b) Sample 2, (c) Sample 3, (d) Sample 5, (e) Sample 6, and (f) Sample 7, as a function of temperature.*

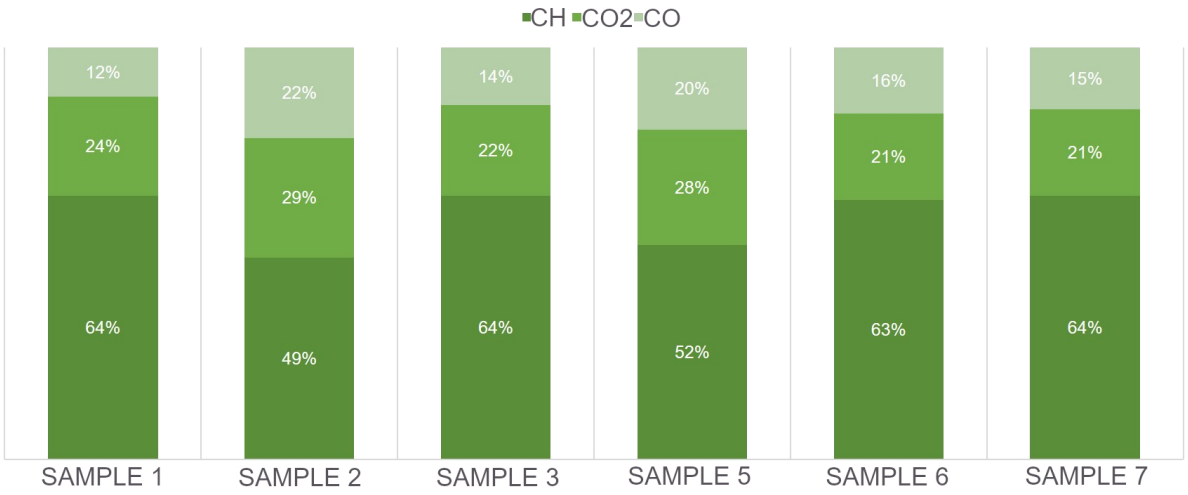

Figure 4.12: *Diagram showing the calculated maximum relative concentrations of the major species, for all the measured samples. As can be seen, the gas mixtures consist mainly of CH, with smaller amounts of CO_2 and CO.*

in combustion processes, usually is the other way around. As mentioned earlier, the simultaneous appearance of the >C=O and CH groups strongly suggests the forming of different aldehydes and ketones, such as formaldehyde, acetaldehyde and acetone. It was also expected that the gasification process would produce lower concentrations of larger hydrocarbons than the pyrolysis process, since the hydrocarbons in the gasification process react to form other species.

A disclaimer regarding the gasification measurements needs to be added: due to the heating wire breaking in the latter stages of the project, measurements could not be performed on Sample 4. Data on the gasification process for this sample are therefore missing. Also, in order to be able to observe both CO_2 and CH, the spectrometer grating had to be rotated to accommodate for another wavelength range. Therefore, the H_2O signal - and possible traces of -NH_2 groups - could not be observed.

Chapter 5

Outlook

RS is known to be a versatile tool for simultaneous multi-species detection, as it is an in situ and non-intrusive diagnostic tool, making it an excellent choice for the characterization of the species formed during biomass pyrolysis and gasification. Compared to other methods, such as mass spectroscopy and gas chromatography, RS has the benefit that the tars formed does not clog any sensitive equipment. Another method worth considering is absorption Fourier transform infrared spectroscopy, which could be used as a complimentary method. It does, however, have a few drawbacks, such as being sensitive to residues and requiring a long probe length.

The major drawback of RS is the low SNR. Therefore, future studies would benefit from utilizing a more sophisticated form of background suppression, or possibly simultaneous background fluorescence recording and subtraction, since the pyrolysis and gasification environments are quite turbulent. It might also be beneficial to use longer excitation wavelengths, e.g., by using a tunable dye laser, as this would give lower LIF from large hydrocarbons by moving the photon energy further away from that of electronic transitions. However, it would also decrease the signal strength significantly since the Raman cross section is proportional to λ^{-4}, but some sort of compromise could probably be reached. Another way to improve the SNR could be to change to another type of heating cell, with a gas flow that encourages a faster ventilation of the formed tars, thus decreasing the background fluorescence.

Since the O_2 concentration in the gasification process was on the lower side (4%, corresponding to 20% of the O_2 concentration in ambient air), and gasification usually utilizes an O_2 concentration in the range 20-30%, it could, in future measurements, be of interest to observe how an increase of this concentration affects the composition of the formed species. Also, the traces of some -NH_2 group found in some of the samples during the lower pyrolysis temperatures were an interesting addition which could be studied further in the future, as a way to more thoroughly characterize the emitted species and the formation of NO_X. The >C=O and CH groups formed during gasification could be studied further - together with area of the -NH_2 group - using a finer grating, to produce

high-resolution spectra. These would be highly beneficial for the characterization of the exact aldehyde and ketone species formed during the process.

References

[1] International Energy Agency, "Key World Energy Statistics", p. 6, 2017.

[2] Swedish Energy Agency, "Energiläget 2017", p. 5, 2017.

[3] World Bioenergy Association, "WBA Global Bioenergy Statistics 2016", p. 30, 2016.

[4] G. Liu, E. Larson, R. Williams, T. Kreutz and X. Guo, "Making Fischer-Tropsch Fuels and Electricity from Coal and Biomass: Performance and Cost Analysis" *Energy & Fuels*, vol. 25, no. 1, pp. 415-437, 2011.

[5] P. Basu, *Biomass gasification and pyrolysis: practical design and theory*, Burlington, MA: Academic, 2010.

[6] A. Demirbas and G. Arin, "An Overview of Biomass Pyrolysis", *Energy Sources*, vol. 24, no. 5, pp. 471-482, 2002.

[7] T. Kan, V. Strezov and T. Evans, "Lignocellulosic biomass pyrolysis: A review of product properties and effects of pyrolysis parameters", *Renewable and Sustainable Energy Reviews*, vol. 57, pp. 1126-1140, 2016.

[8] E. Björkman and B. Strömberg, "Release of Chlorine from Biomass at Pyrolysis and Gasification Conditions", *Energy & Fuels*, vol. 11, no. 5, pp. 1026-1032, 1997.

[9] A. Bridgwater, "The Technical and Economic Feasibility of Biomass Gasification for Power Generation", *Fuel*, vol. 74, no. 5, pp. 631-653, 1995.

[10] S. Karellas and J. Karl, "Analysis of the product gas from biomass gasification by means of laser spectroscopy", *Optics and Lasers in Engineering*, vol. 45, no. 9, pp. 935-946, 2007.

[11] Kopiersperre, *Gasifier types*, (adapted from original) used under CC-BY-SA-3.0, 2014. URL: `https://commons.wikimedia.org/wiki/File:Gasifier_types.svg`

[12] A. Eckbreth, *Laser diagnostics for combustion temperature and species*, 2nd ed. Amsterdam: Gordon & Breach, pp. 209-273, 1996.

[13] C. Banwell and E. McCash, *Fundamentals of molecular spectroscopy*, 4th ed. Berkshire: McGraw-Hill Publishing Company, pp. 86, 100-125, 1994.

[14] S. Eichmann, M. Weschta, J. Kiefer, T. Seeger and A. Leipertz, "Characterization of a fast gas analyzer based on Raman scattering for the analysis of synthesis gas", *Review of Scientific Instruments*, vol. 81, no. 12, p. 125104, 2010.

[15] H. Johansson, "Development of optimized Raman Spectroscopy setup for species detection in flames", B.Sc., Lund University, 2016.

[16] K. Davidsson, P. Atonga, C. Haraldsson, D. Künemuth, T. Richards, E. Sahlin, H. Thunman, "Bränsleanalys för förgasning", Göteborg Energi, Gothenburg, 2013.

[17] T. Leffler, "Bränsleanalyser", Vattenfall Research and Development, 2018. [email]

[18] T. Shimanouchi, *Tables of Molecular Vibrational Frequencies: Consolidated volume I*, National Bureau of Standards, 1972.

[19] G. Xu, X. Fan and A. Miller, "Plant Nitrogen Assimilation and Use Efficiency", *Annual Review of Plant Biology*, vol. 63, no. 1, pp. 153-182, 2012.

[20] K. Nadelhoffer, J. Aber, J. Melillo, "Seasonal patterns of ammonium and nitrate uptake in nine temperate forest ecosystems", *Plant and Soil*, vol. 80, no. 3, pp. 321-335, 1984.

[21] V. Smil, *Cycles of life*. New York: Scientific American Library, 2000.

[22] T. Milne, R. Evans and N. Abatzoglou, *Biomass Gasifier "Tars": Their Nature, Formation, and Conversion*. Golden, Colo.: National Renewable Energy Laboratory, p. 5, 1998.

[23] G. Magnotti, U. KC, P. Varghese and R. Barlow, "Raman spectra of methane, ethylene, ethane, dimethyl ether, formaldehyde and propane for combustion applications", *Journal of Quantitative Spectroscopy & Radiative Transfer*, vol. 163, pp. 80-101, 2015.

[24] C. Brackmann, "Development and Application of Rotational Coherent Anti-Stokes Raman Spectroscopy and Laser-induced Fluorescence for Combustion Diagnostics", Ph.D., Lund Institute of Technology, 2004.

Acknowledgments

Acknowledgments are due, first and foremost, to my supervisor, Christian Brackmann, for giving me the opportunity to work on this project and for his support during its course. Thanks are also due to Haisol Kim, Jim Larsson and Miaoxin Gong, for all the help provided in setting up equipment, performing measurements and post-processing of the data. In addition, I would like to show my appreciation to all the people at the division of combustion physics that made the time that I spent there enjoyable.